Journal of Advanced Joining Processes 5 (2022) 100096

Contents lists available at ScienceDirect

Journal of Advanced Joining Processes

journal homepage: www.sciencedirect.com/journal/journal-of-advanced-joining-processes

On weldability of aerospace grade Al-Cu-Li alloy AA2065 by wire-feed laser metal deposition

Siri Marthe Arbo *, Stanka Tomovic-Petrovic, Jo Aunemo, Nora Dahle, Ola Jensrud

Department of Materials Technology, SINTEF Manufacturing, Raufoss, NO-2831 Norway

ARTICLE INFO

Keywords:
Laser metal deposition
Wire
Al-Cu-Li alloys
Aerospace
Process parameters

ABSTRACT

Al-Cu-Li alloys exhibit a superior strength to weight ratio, making the alloys attractive for applications within aviation and aerospace. However, their widespread application has been somewhat limited by the challenges associated with porosity and crack formation during welding. The purpose of this study was to evaluate the weldability of aerospace grade Al-Cu-Li alloy AA2065 by wire-based Laser Metal Deposition (LMD) by using a self-produced wire. The influence of selected process parameters on deposition geometry (width, height and deposition depth), porosity, microstructure and hardness were evaluated by producing single tracks on a base plate. Defect-free tracks with minimal porosity could be produced with a laser power of 2700 W, 800 μm spot size and 1 m/min scanning speed, providing an energy density of 5.4 J/mm^2. Depending on the desired deposition rate, the wire-feed rate could be varied between 1 and 1.9 m/min. The microstructure of the deposited material consisted of columnar and globular equiaxed grains with a Cu-rich second phase network throughout the deposited material. The results presented in this study show the potential in utilizing wires produced of AA2065 for laser welding and potentially additive manufacturing by wire-based LMD, increasing the possible areas of application for such high-strength, low weight alloys.

Introduction

In recent years, aluminum-copper-lithium (Al-Cu-Li) alloys have been highlighted as one of the most promising alloys for structural applications within the aviation and aerospace industry (Rioja and Liu, 2012; Ahmed and Wu, 2014; Dursun and Soutis, 2014). The Al-Cu-Li alloys offer a high strength, high stiffness and resistance against fatigue fractures, in addition to a large reduction in weight (Rioja and Liu, 2012; Dursun and Soutis, 2014). The addition of 1 wt% Li to Al reduces the density of the alloy by 3% and increases the modulus of elasticity by 6% (Rioja and Liu, 2012), giving the alloy improved mechanical properties compared to existing alloys used for structural components. The newly developed third-generation Al-Cu-Li alloys (AA2195, AA2099 and AA2065) consists of a low Li content (<2 wt%), while maintaining a Cu content of typically > 2 wt%. In addition, small additions of alloying elements, such as magnesium (Mg) and silver (Ag) are added to help achieve the superior mechanical properties (Rioja and Liu, 2012; Abd El-Aty et al., 2018; Gumbmann et al., 2017). The AA2195 alloy has for instance been used for the propellant tank on NASA's Space Shuttle. The alloy is 30% stronger and has a 5% lower density than the originally used AA2219 alloy, allowing the space shuttle to carry heavier components (National Aeronautics and Space Administration, 2005).

To increase the application of aluminum in structural components, weldability is of high importance. The aerospace grade 2xxx and 7xxx alloys are known for their susceptibility to cracking and porosity formation during traditional fusion welding, which have limited their areas of application (Campbell Jr, 2011). As part of the 2xxx classification, the same challenges also apply for the Al-Cu-Li alloys (Madhusudhan Reddy and Gokhale, 2014). In addition to cracking and porosity, the formation of a Heat Affected Zone (HAZ) adjacent to the weld, caused by microstructural changes is an additional challenge that must be controlled during welding of aluminum alloys in general (Campbell Jr, 2011; Madhusudhan Reddy and Gokhale, 2014; Xiao and Zhang, 2014). Çam and İpekoğlu (Çam and İpekoğlu, 2016) reviewed the recently developed techniques for welding of aluminum alloys, such as laser welding, focusing on porosity, cracking, resulting microstructure and mechanical properties. The laser-based welding techniques have in recent years been demonstrated to be a promising technique for welding of aluminum alloys, including the challenging 2xxx and 7xxx alloys. The technique involves using a highly concentrated heat source, which

* Corresponding author.
E-mail address: siri.marthe.arbo@sintef.no (S.M. Arbo).

https://doi.org/10.1016/j.jajp.2022.100096
Received 11 November 2021; Received in revised form 5 January 2022; Accepted 5 January 2022
Available online 7 January 2022

reduces the total heat input compared to traditional welding techniques, resulting in a narrow HAZ, in addition to little welding deformation and high process efficiency (Xiao and Zhang, 2014; Çam and İpekoğlu, 2016). Nevertheless, cracking and porosity are still challenging to overcome even with the laser-based welding techniques (Xiao and Zhang, 2014).

One approach to reduce porosity and susceptibility to cracking is by using filler wires during welding. Zhang, H et al. (Zhang et al., 2016) showed that by using an Al-Si12 filler wire, AA2060 plates could successfully be welded together by laser beam welding, obtaining 80% strength of the base material. In addition, no porosity or cracking was observed. Similarly, Zhang, T. et al. (Zhang et al., 2020) successfully laser welded together an AA2060 and AA2099 plate using an Al-Si filler wire. Nevertheless, studies have also shown that laser welding of Al-Cu-Li alloys is possible even without filler wires. Already back in 1990, Molian and Srivatsan (Molian and Srivatsan, 1990) demonstrated that AA2090 plates could be welded together with a high energy laser source, achieving a low degree of porosity by applying argon gas shielding. More recently, Gu et al. (Gu et al., 2016) performed laser beam welding of AA2060 plates. Welding porosity existed in the microstructure and only a strength reaching 67.9% of the base metal could be achieved. The importance of finding the right process parameters was demonstrated by Liu et al. (Liu et al., 2017), stating that both porosity and cracking susceptibility was strongly influenced by the welding speed and laser power for AA2198/AA2060 dissimilar welds.

Laser-based welding techniques can also be used for additive manufacturing. In recent years, only a handful of articles have investigated the possibilities of using Al-Cu-Li alloys for additive manufacturing. Zhong et al. (Zhong et al., 2019) for instance showed that a self-produced AA2050 wire could be successfully applied for wire arc additive manufacturing, achieving a crack-free component with minimal porosity after process optimization.

More research is necessary to fully investigate the potential of the Al-Cu-Li alloys within welding and additive manufacturing, and especially for wire-based techniques. Thus, the current work focuses on the weldability of the AA2065 alloy, which has to the authors knowledge not been previously studied. The goal was to investigate if a self-produced AA2065 wire could be utilized for wire-feed LMD. The influence of selected process parameters on the resulting deposition characteristics has been investigated. The work provides a basis for further investigations into additive manufacturing and welding of these alloys using wire-based techniques.

Materials and methodology

Materials

An AA2065 wire was produced through extrusion and wire-drawing with subsequent annealing heat treatments (410 °C for 2 h) by SINTEF Manufacturing together with KA Rasmussen, from an extruded billet from Constellium. The produced wire had a diameter of 1.2 mm and was used in the as-fabricated condition. The wire contained some shallow surface wounds after the production as shown in Fig. 1(a). The wire consisted of several small particles, homogeneously distributed in the structure, see Fig. 1(b).

A 30 mm thick AA7475 plate was chosen as the base material, with an initial hardness of 160 HV0.5. The chemical composition of the wire and the base material is presented in Table 1. Prior to the deposition procedure, the wire and base plate were cleaned thoroughly with acetone.

Laser metal deposition procedure

Single-track deposits with a length of 50 mm were produced on the base material using a Trumpf TruLaser Cell 3000 LMD machine equipped with a 3000 W fiber laser. The experimental setup is presented in Fig. 2, comprised of an angled laser housing, shielding gas nozzle and wire feeder.

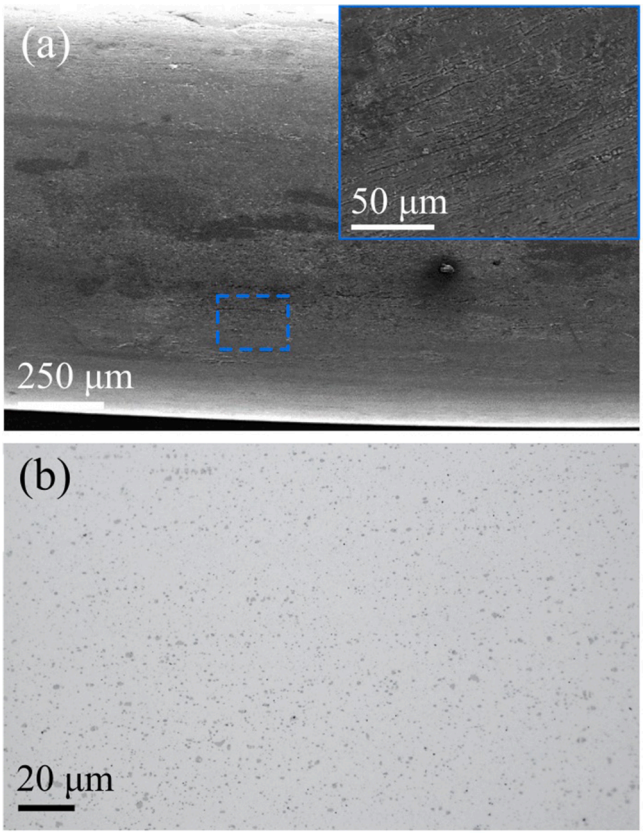

Fig. 1. (a) SEM images of the surface of the AA2065 wire. (b) Particle distribution in wire cross section.

The wire was fed in the front of the laser during the deposition process. Argon was used as shielding gas, positioned at an angle in regard to the wire-feeding, as illustrated in Fig. 2. The laser beam is generated with a 400 µm fiber, rectangular pulse, without cross-jet function with a frequency of 5010 Hz. The focal point was kept at the base plate surface for all the experiments.

The remainder process parameters were varied during the deposition and are listed in Table 2 for each deposited track.

Characterization

The surface characteristics and cross-sections of the produced single LMD tracks were afterwards studied in detail. The surface characteristics were investigated by an Olympus SZX10 stereomicroscope, investigating the track morphology and deposition width. Cross-sections parallel and perpendicular to the scanning direction were ground and polished using standard metallographic procedures. The cross-sections were first investigated using a Zeiss Axio Observer optical microscopy, evaluating the porosity, and measuring the molten pool depth and deposition height of each track. A minimum of 3 cross-section were investigated for each track. The particle distribution was investigated using a Hitachi S-3500 N Scanning Electron Microscopy (SEM), operated at 20 kV, and a working distance of 15 mm. An Oxford Instrument X-Max 80 detector was used to obtain Energy-dispersive X-ray Spectroscopy (EDS) maps of selected regions of the deposited track.

The microstructure was investigated by anodization the cross-sections of the deposited tracks with Barkers Reagent (5% HBF_4 in water, 20 V for 60 s) after polishing and studying the specimen using polarized light.

Vickers hardness measurements were obtained on a ground cross-

Table 1
Chemical composition [wt%] of AA2065 wire and AA7475 base material.

	Cu	Li	Mg	Fe	Si	Mn	Cr	Zn	Zr	Ag	Al
AA2065-F	4.4	1.02	0.33	0.05	0.02	0.38	–	0.13	0.06	0.3	Bal.
AA7475-T74	1.45	–	2.2	0.12	0.1	0.06	0.22	5.9	0.03	–	Bal.

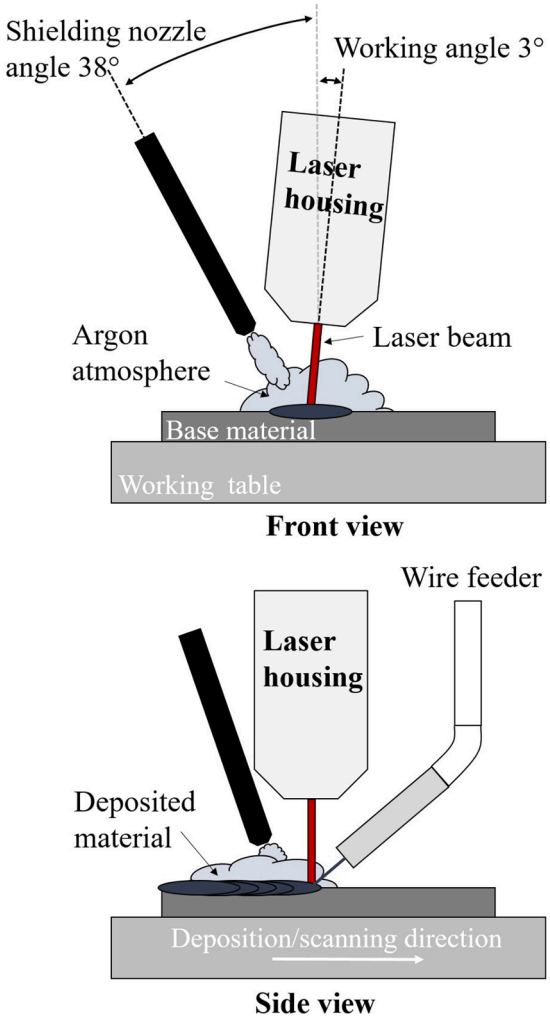

Fig. 2. Schematic illustration of the LMD set-up, showing the position of the laser beam, wire feeder and shielding gas nozzle during the process.

section using a Tukon 2500 machine (HV0.5) within a week after welding. The measurements were obtained through the center of the track and into the base material, with a distance of 500 μm between each indent.

Results and discussion

Track morphology with increasing laser power

To investigate the influence of each process parameter on deposition geometry and characteristics, single tracks were produced, variating one process parameter at a time, as listed in Table 2. A continuous track on the base material surface was produced for all the investigated process parameter combinations. The surfaces of the tracks produced with laser power of 2600 W, 2700 W and 2800 W are presented in Fig. 3(a), (c) and (e), respectively. The process parameters used for each track and the corresponding energy density (E [J/mm^2]) is listed in the figure. Keep in mind that the spot size was not changed during the trials.

Table 2
Process parameter combinations investigated in the current study.

Track	Process parameters				
	Laser power, P [W]	Wire-feed rate, V_w [m/min]	Scanning speed, V_s [m/min]	Shield gas rate, GR [L/min]	Spot size [μm]
#1	2600	1.7	1	15	800
#2	2700	1	1	15	800
#3	2700	1.5	1	15	800
#4	2700	1.7	1	15	800
#5	2700	1.9	1	15	800
#6	2800	1	1	15	800
#7	2800	1.5	1	15	800
#8	2800	1.7	1	15	800
#9	2800	1.9	1	15	800
#10	2800	2	2	15	800
#11	2800	2.5	2	15	800
#12	2800	3	3	15	800
#13	2800	1.9	1	10	800
#14	2800	1.9	1	17	800

For laser power of 2600 W, the heat input was too low to sufficiently melt the wire and thus, the wire was only deposited on top of the base material, made clear by Fig. 3(a) and Fig. 3(b). By increasing the laser power to 2700 W and 2800 W and the corresponding energy density to 5.4 and 5.6 J/mm^2, respectively, the available heat could sufficiently melt both the wire and the surface of the base material, successfully creating continuous deposited tracks, seen in Fig. 3(c) and (e). The cross-sections of these tracks are presented in Fig. 3(d) and (f). An increasing width of the deposited track is also observed with increasing heat input. It should be noted that the influence of the wire-feed rate was not investigated and that for lower wire-feed rates, continuous tracks might be achieved with a lower heat input i.e., with an energy density of 5.2 J/mm^2.

From Fig. 3(c) and (e), it is clear that the surface of the deposited tracks is irregular, with clear striation marks going perpendicular to the scanning direction. The roughness of the striation marks appears to be increasing with increasing laser power, see Fig. 3(a), (c) and (e). Such striation marks, also referred to as ripples by Xu et al. (Xu et al., 2017), was observed to form during LMD of steel when the heat input was too high compared to the wire-feed rate. The high heat input causes wire dripping, i.e., a discontinuous deposition of the wire, creating ripples on the surface. Thus, an excessive heat input and the corresponding surface rippling, makes the process undesirable for additive manufacturing applications. In addition, an unstable process could result in undesirable welding defects, such as lack of fusion, increased porosity formation or consequently stresses in the final deposited material.

Thus, for the AA2065 wire, the optimal laser power for the scanning speed and wire-feed rate applied in this study should be around 2700 W. This means that an energy density of 5.4 J/mm^2 is needed to ensure a sufficient heat input for melting of both the wire and base material, and at the same time reduce the formation of ripples on the surface.

Effect of process parameters on geometry of deposited tracks

The relationship between the investigated process parameters and the geometry (width, height and depth) of the deposited tracks are presented in Fig. 4(b)–(d). The measurements were obtained from the polished cross-sections of the deposited tracks, as illustrated in Fig. 4(a). All other process parameters were kept constant during the evaluation of

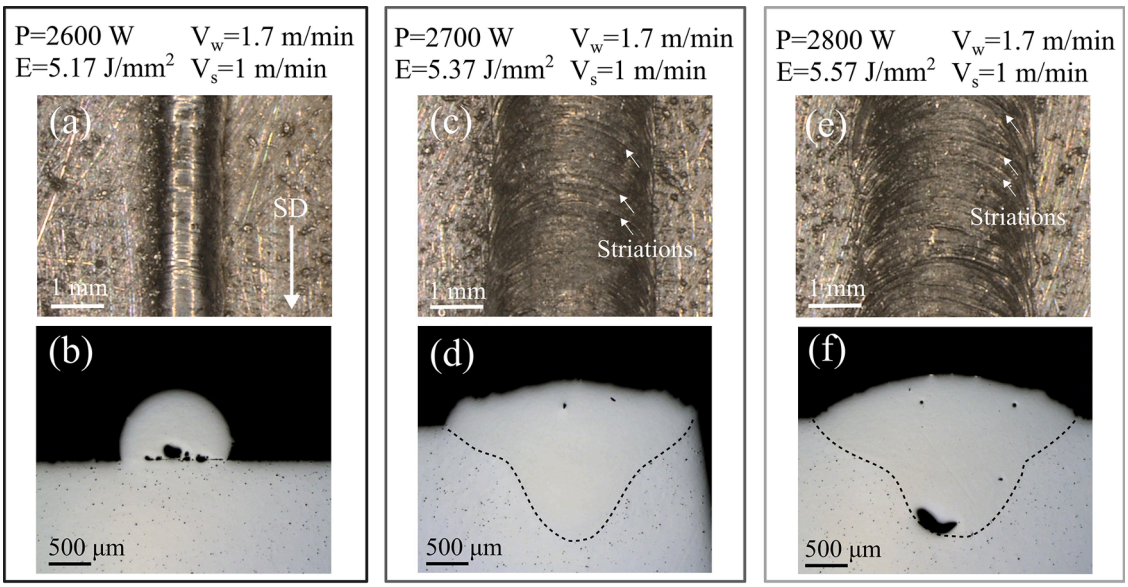

Fig. 3. Influence of laser power (P). (a)–(b): 2600 W, (c)–(d) 2700 W and (e)–(f) 2800 W, on track morphology and characteristics of deposited material. SD=Scanning direction, V_w = wire-feed rate, V_s = Scanning speed, E = Energy density.

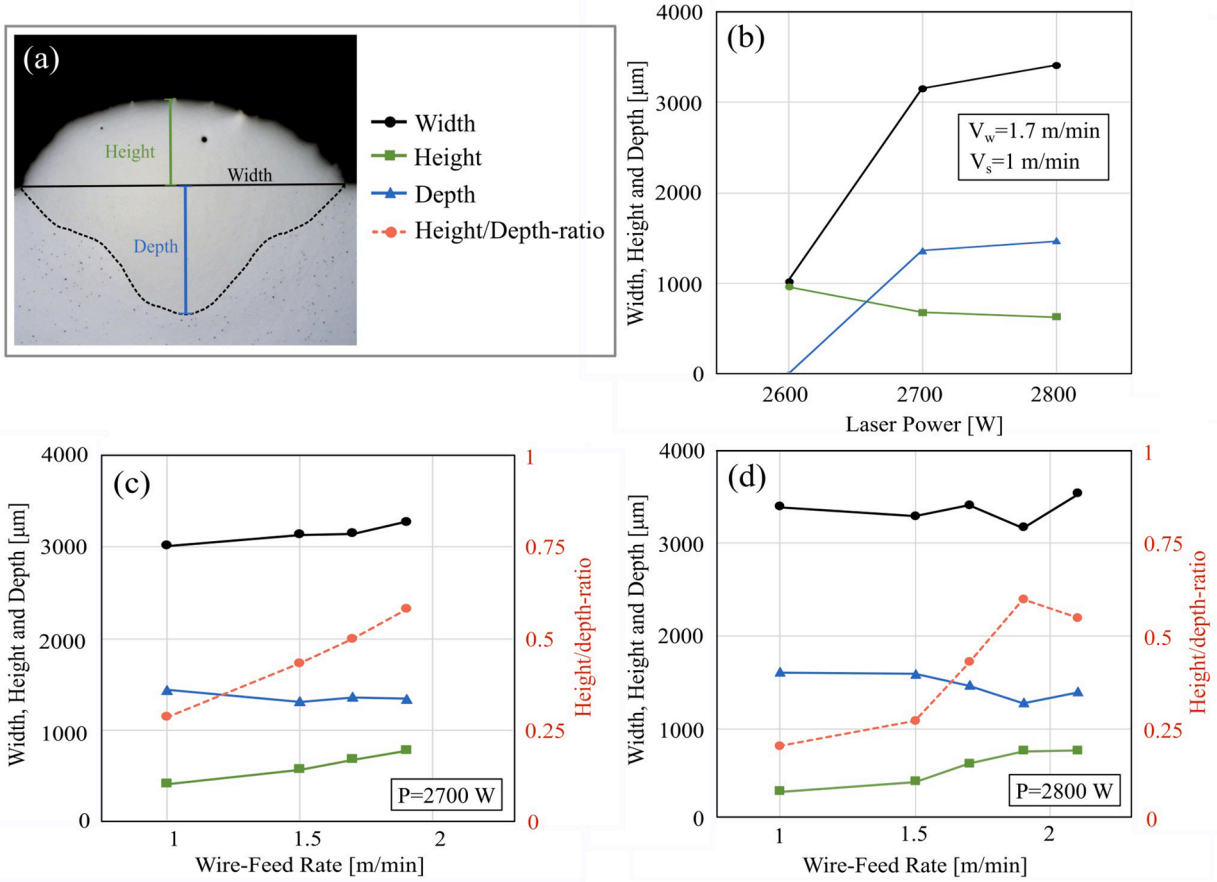

Fig. 4. Effect of process parameters on the geometry of deposited track (width, height and deposition depth). (a) Cross-section of the deposited track and defined labels. (b) Influence of laser power, P with constant wire-feed rate, V_w and scanning speed, V_s. Influence of wire-feed rate at (c) 2700 W and (d) 2800 W with constant scanning speed, V_s = 1 m/min.

the laser power and the wire-feed rate.

The geometry of the deposited tracks is important in terms of application. The height and width are for instance important parameters when planning the build strategy during additive manufacturing, affecting the optimum bead spacing and necessary height adjustment during subsequent layer deposition, discussed in the work by Froend et al. (Froend et al., 2018). Thus, a high height/depth-ratio is for instance beneficial for the subsequent layer deposition in additive

manufacturing, as it allows for high building rates.

Laser power

It is clear from the results in Fig. 4(b) that the influence of the laser power on the track geometry is significant. With laser power of 2600 W, the wire and base material did not fuse together, depositing the wire on top of the base material, indicated in Fig. 4(b) and shown previously in Fig. 3(b). From Fig. 4(b) it can be observed that with increasing laser power, the width and deposition depth increase. At the same time, the height decreases.

A higher laser power results in a slower solidification due to a higher heat input and higher energy density, as presented previously in Fig. 3. Thus, the material is able to flow outwards before solidifying, resulting in an increased width and decreased height. Also, a higher laser power supplies more heat to melt the base material, allowing for a deeper penetration depth. Similar trends have been found in other studies when evaluating the influence of increasing laser power on deposition geometry during laser welding for both aluminum wires and powders (Gu et al., 2016; Caiazzo et al., 2017; Huang et al., 2021; Jiao et al., 2020). A laser power of around 2700 W or higher, equal to an energy density of 5.4 J/mm^2 with scanning speed 1 m/min, is needed when performing LMD with a 1.2 mm AA2065 wire to achieve a sufficient fusion with the base material. This supports the hypothesis stated earlier based on the observed track morphology.

Wire-feed rate

The influence of the wire-feed rate on track geometry with laser power 2700 W and 2800 W are presented in Fig. 4(c) and (d), respectively. Based on the initial evaluation of scanning speed vs wire-feed rate, a scanning speed of 1 m/min was chosen during the evaluation of wire-feed rate. It can be observed that for a constant laser power and scanning speed, the depth of the track decreases, while the height increases, with increasing wire-feed rate. Overall, the tracks deposited with a laser power of 2800 W have a slightly larger depth and width compared to the tracks deposited with 2700 W, due to the higher energy density available with larger laser power. This correspond to previous results presented by Huang et al. (Huang et al., 2021). With increasing wire-feed rate, the amount of material to be melted increases, reducing the heat available for melting the base material. Thus, the material is deposited on top of the base material to a larger extent. This argument is supported by the increasing height/depth-ratio with increasing wire-feed rate, see Fig. 4(c) and (d). A high height/depth-ratio is desirable when performing for instance additive manufacturing, allowing for a high building rate.

During the investigation, it was found that if the wire-feed rate became too fast compared to the scanning speed, the heat could not sufficiently melt the wire. Hence, the wire was pushed into the melt pool, terminating the process. For 2700 W and 2800 W, a wire-feed rate above 1.9 m/min and 2.1 m/min was found to be maximum when using a 1 m/min scanning speed, respectively. Higher wire-feeding reates were therefor not investigated.

Microstructure of deposited tracks

Fig. 5(a) shows a micrograph of the cross-section of a deposited track obtained with polarized light after anodization. The observed microstructure was similar among the tracks, independent of process parameters. High magnification images of the two areas highlighted in (a) are presented in Fig. 5(b) and (c).

Two types of grain morphologies can be observed. First, along the fusion line, the microstructure consists of elongated coarse grains growing from the fusion line and into the deposited material, Fig. 5(b). The grains grow in the direction of the largest thermal gradient. Secondly, in the center of the deposited track, the microstructure consists of globular equiaxed grains, due to the change in cooling rate experienced in this area of the deposited track. The observed microstructure is commonly observed in deposited aluminum using wire and/or laser techniques (Xiao and Zhang, 2014; Gu et al., 2016; Liu et al., 2017; Zhong et al., 2019; Caiazzo et al., 2017; Huang et al., 2021). Thus, the results correspond well with the established knowledge on microstructural formation with this manufacturing technique. The grain morphology does not appear to have changed in the HAZ of the base material, adjacent to the fusion boundary, i.e., over-aging is the reason for the measured lower hardness in this zone, see section 3.4, not the microstructure.

The microstructure of the two areas was studied more in detail at higher magnification, see Fig 5(d) and (e). These analyses revealed the presence of an intragranular second phase network, which could easily be observed on the anodized specimens. No clear accumulation of phases along the grain boundaries could be observed when studying the specimens in both optical microscope and during SEM analysis. To confirm which elements that constitutes this network, EDS element mapping was performed, shown in Fig. 6(a) and (b) for the fusion line and center positions, respectively. Li is not detected with EDS analysis due to the low emission energy and low atomic weight and hence not included in the figure. The maps revealed that the semi-coherent second

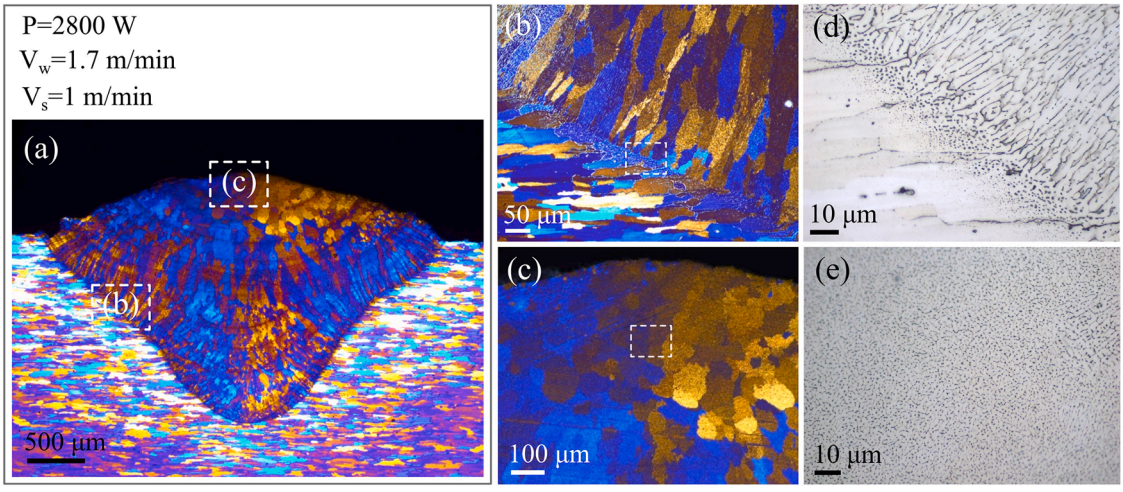

Fig. 5. (a) Micrograph of the cross-section of one deposited track, showing the generally observed microstructure. Areas highlighted in (a) are presented in (b) and (c), showing the fusion boundary and the center of the track, respectively. The corresponding high magnification images are given in (d) and (e), respectively. P = laser power, V_w = wire-feed rate, V_s = scanning speed.

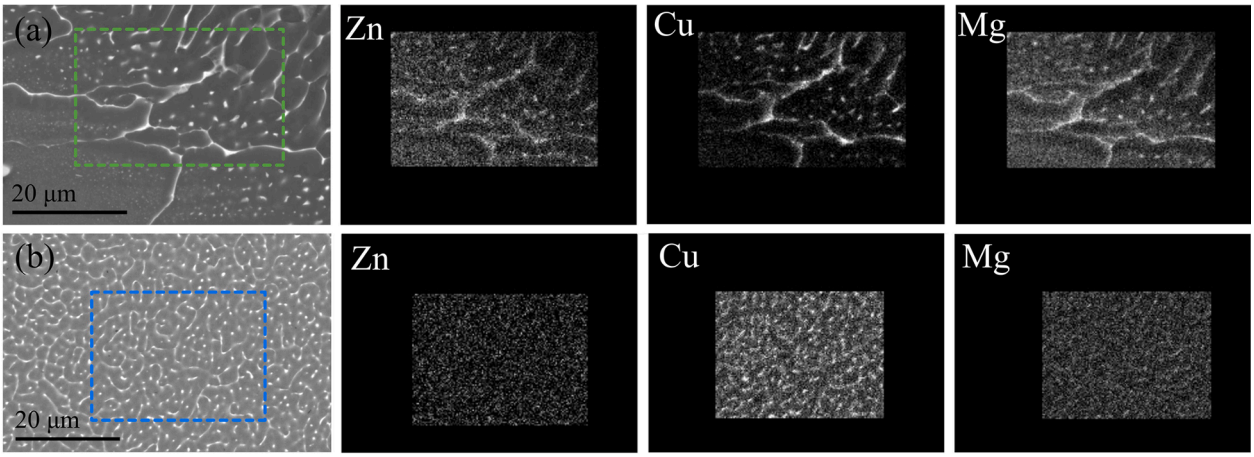

Fig. 6. SEM images and corresponding EDS element map for alloying elements Zink (Zn), Copper (Cu) and Magnesium (Mg) for (a) along the fusion boundary and (b) center of the deposited track.

phase network is rich in Cu in both position, see Fig 6(a) and (b). A long the fusion line, Fig 6(a), the phase is also enriched with both Zn and Mg, stemming from the high Zn (5.9 wt%) and Mg (2.2 wt%) content of the AA7475 base material. Little Cu was detected in the Al-matrix. Thus, in this region, alloying elements from both the base material, AA7475 and the wire, AA2065 have contributed to the phase formation along the grain boundaries.

The Al-Cu-Li alloys with high Cu content, such as AA2065 are reported to consist mainly of θ'-Al_2Cu, T_1-Al_2CuLi, T_2-Al_6CuLi_3 and δ'-Al_3Li precipitates, which provides the high strength and toughness (Rioja and Liu, 2012; Ahmed and Wu, 2014; Abd El-Aty et al., 2018; Liu et al., 2017). Originally in the wire, two Cu-rich phases were observed, both with a Cu content fitting with the eutectic composition in the binary Al-Cu phase diagram, suggesting it would be θ'-Al_2Cu together with one Al-Cu-Li phase. The same is observed for the secondary phase network formed after deposition. A similar network has been observed during microstructural investigations of the welded interfaces or in the deposited material during additive manufacturing of Al-Cu-Li and Al-Cu alloys in the literature (Liu et al., 2017; Zhong et al., 2019; Caiazzo et al., 2017). Zhong et al. (Zhong et al., 2019) concluded that the secondary phase was Al_2Cu, in addition to Al_3Li, by XRD analyses. Since Li cannot be detected by EDS, more in-depth characterization for instance by TEM is necessary in order to fully characterize the particles present in the wire and the deposited material. The formed phases and precipitates are also sensitive to the thermomechanical process (Zhong et al., 2019; Jiao et al., 2020) and future work should focus on understanding the phase formation during additive manufacturing and welding followed by post-welding heat treatment, in order to optimize the mechanical properties.

Microstructure of deposited tracks

Solidification cracking

The relationship between the scanning speed and wire-feed rate strongly influence porosity formation and material deposition rate for wire-based LMD, as demonstrated by Ryan et al. (Ryan et al., 2018). In the current study, tracks were deposited with a 1:1 and 1.5:1 relationship between the scanning speed and the wire-feed rate, to further investigate this relationship, see Table 3. Cross-sections for two of the tracks listed in Table 3 are presented in Fig. 7(a) and (b). Images at higher magnification of the crack is shown in Fig. 7(c) and (d), where (c) shows the grain structure and (d) the particle structure. When keeping a 1:1 relationship between the scanning speed and wire-feed rate, a crack free track was produced for values of 1 m/min, Fig 7(a). When increasing the values to 2 and 3 m/min, solidification cracking in the center of the deposited track was observed.

Table 3
Process parameters and appearance of deposited track (#).

#	P [W]	V_w [m/min]	V_s [m/min]	Comment
#6	2800	1	1	Ok
#7	2800	1.5	1	Ok
#10	2800	2	2	Fracture
#11	2800	2.5	2	Ok
#12	2800	3	3	Fracture

The cracks propagated along the grain boundaries as shown in Fig. 7 (c). In the center region of the deposited material, the observed secondary phase network is intragranular, with no clear accumulation of alloying elements along the grain boundaries, as presented in the previous section. Thus, the formed phase network is not the cause of the fracture. However, with a higher scanning speed, the material is experiencing high levels of thermal stress and solidification shrinkage. This promotes a strong solidification texture, which again promotes solidification cracking, typically in the center of the weld (Xiao and Zhang, 2014; Çam and İpekoğlu, 2016) as seen in track #10, Fig. 7(b)–(d).

When the wire-feed rate was increased to 2.5 m/min, a crack-free track could be deposited with scanning speed of 2 m/min. The increased wire-feed rate supplied the weld with a sufficient amount of material to help avoid cracking during solidification. Thus, a 1:1 relationship between the wire-feed rate and scanning speed can only produce deposited tracks without cracks when kept at 1 m/min.This is a result of the reduced heat input and increased cooling rate achieved when increasing the scanning speed from 1 to 2 and 3 m/min (Caiazzo et al., 2017). Thus, a low scanning speed can suppress cracking during solidification.

A similar observation was also made by Liu et al. (Liu et al., 2017). Pre-heating of the base material could also be beneficial for reducing the thermal stresses in the deposited material, allowing for higher scanning speeds to be applied during LMD (Froend et al., 2018).

The AA2065 alloy contains manganese and zirconium, which are added to promote dispersoid formation (Rioja and Liu, 2012; Gumbmann et al., 2017). This additions of small amounts of manganese and zirconium (Kim et al., 1996), in addition to keeping the copper content above 4 wt% (Madhusudhan Reddy and Gokhale, 2014), has been reported to help reduce the alloys susceptibility to cracking. Thus, for the AA2065, the chemical composition combined with the optimization of wire-feed rate and scanning speed facilitates the alloys weldability.

Porosity

Overall, the cross-sections studied of the deposited tracks revealed

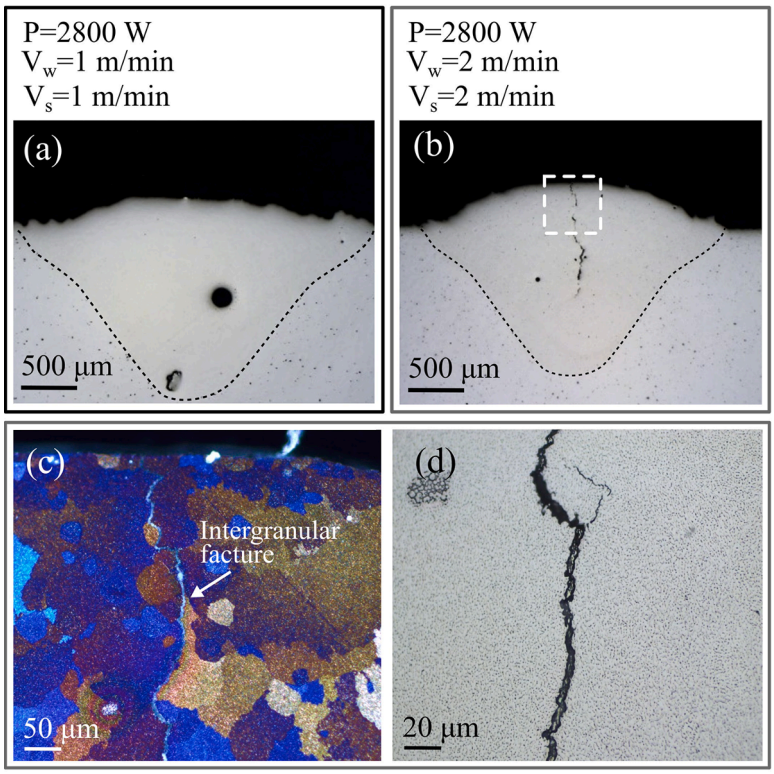

Fig. 7. Relationship between scanning speed, V_s and wire-feed rate, V_w on cracking. Cross-section of specimen (a) #6 (b) #10. (c) obtained with polarized light showing the intergranular fracture highlighted in (b). (d) High magnification image showing the particle structure and fracture.

little or no porosity. However, as seen in Fig. 3(f) and Fig. 7(a), pores were occasionally observed. To further investigate the porosity formation, cross-sections taken parallel to the scanning direction were polished and examined. Images of selected tracks are shown in Fig. 8(a)-(h), showing the influence of laser power, wire-feed rate and shield gas rate on porosity formation.

In general, the observed pores are spherical, and for the most part located towards the bottom, close to the fusion line in the deposited track. Metallurgical porosity due to hydrogen porosity is common in welded aluminum structures, as the weld pool absorbs hydrogen when

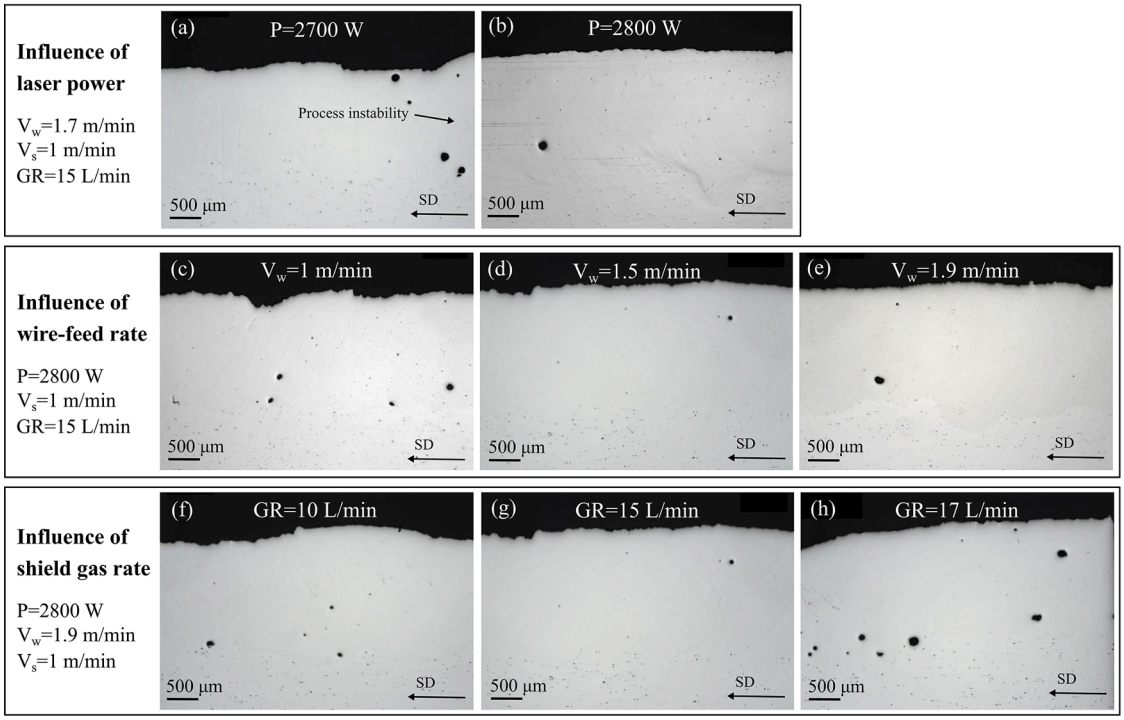

Fig. 8. Cross-section parallel to the scanning direction for tracks deposited with different process parameters to investigate the effect on porosity formation. (a) and (b): influence of laser power, P. (c)–(e): influence of wire-feed rate, V_w. (f)–(h): influence of shield gas rate, GR. Scanning speed, V_s was kept constant.

in a liquid state. However, the solubility of hydrogen decreases rapidly with decreasing temperature. Thus, during the rapid cooling, hydrogen gets trapped inside the deposited material upon solidification, resulting in the formation of spherical pores (Madhusudhan Reddy and Gokhale, 2014; Xiao and Zhang, 2014; Çam and İpekoğlu, 2016). Gu et al. (Gu et al., 2016) observed that with increasing heat input, porosity formation decreased due to slower cooling rates, allowing the pores to escape prior to solidification of the material. However, a too high heat input increased the porosity formation again. Comparing the number of pores and the process parameters used, no relationship between porosity and laser power can be established in the current study, Fig 8. (a) and (b).

A similar argumentation can be used when discussing the influence of wire-feed rate on porosity. A low wire-feed rate results in a faster cooling rate compared to tracks deposited with a high wire-feed rate, as there is less material to solidify.Qualitative evaluations of the influence of wire-feed rate suggest that a low wire-feed rate of 1 m/min causes a slightly larger degree of porosity, entrapping the hydrogen to a larger extent upon solidifying, Fig. 8(c)–(e).

The influence of the surface quality of the wire during wire arc additive manufacturing on porosity formation was demonstrated by Ryan et al. (Ryan et al., 2018). Notches and a rough surface finish act as sites for contamination, which increases the area covered by the natural oxide layer found on aluminum. This affects the hydrogen content on the wire surface, promoting the formation of porosity. No Al-Cu-Li alloy wire is currently commercially available and thus, the wire used in the current study was produced especially for this study by extrusion followed by wire drawing. SEM images of the surface of the produced wire were shown in Fig. 1. Shallow wounds and scratches were observed. Cleaning of the wire was thoroughly conducted with acetone, to help eliminate any contamination to minimize the risk of porosity formation during deposition. Based on the presented results, the quality of the wire has been sufficient and the small surface wounds have not caused a large degree of porosity.

To further help avoid the absorption of hydrogen during deposition, shielding gas is applied. The flow rate of the shielding gas was kept at 15 L/min for the majority of the trials, based on the low porosity in studies using the same flow rate (Gu et al., 2016; Zhong et al., 2019; Huang et al., 2021).

To investigate the effect of the shielding gas rate on the observed porosity, tracks were deposited with a gas rate of 10 L/min and 17 L/min. Cross-sections for the track produced with the three shield gas rates are shown in Fig. 8(f)-(h), respectively. From the images, it appears that a larger number of pores can be observed in the track deposited with a 17 L/min gas rate compared to the track with 10 and 15 L/min gas rate. If these pores are related to hydrogen or if they are a result of the high shield gas rate is not possible to determine. However, the results show that an excessive gas rate is not optimal and will result in a higher degree of porosity. Keeping the gas rate between 10 and 15 L/min appears to be sufficient for preventing a large degree of porosity during the deposition when the wire is deposited on a substrate plate, as in this study. Additional optimization is necessary when performing for instance groove welding.

As indicated in Fig. 8(a), porosity is observed directly after the hump in the deposited track, caused by a process instability due to uneven wire feeding. The produced wire had some shape irregularities and at some points during the process, the wire moved out of the laser beam focus point, causing an uneven wire-melting and thus, uneven deposition rate allowing the formation of pores.

Hardness

Hardness measurements were obtained along two directions, both inside the deposited track from top to bottom, and parallel from the center of the deposited track and into base material, as illustrated in Fig. 9(a). The measurements were obtained from tracks produced with laser power of 2700 W and 2800 W. AA2065 is a heat treatable alloy, meaning that the mechanical properties, including the hardness are affected by the heating and cooling experienced by the material. After solidification upon depsoition, the alloy has aged naturally (T4) and the hardness measurements were obtained one week after production, representing the as-deposited hardness of the material. The hardness is expected to increase further with time.

Fig. 9(b) show that the hardness increases slightly towards the bottom of the deposited material, from 85 to 90 HV to 100 HV. At the bottom, the AA2065 wire has been substantially mixed with the AA7475 base material and contains a higher degree of alloying elements as part of the second phase network described previously. Hence, this increases the hardness in this region.

The hardness measurements obtained parallel to the base material surface Fig. 9(c), reviled the formation of a HAZ adjacent to the fusion line where the base material has experienced a decrease in hardness. The hardness in the deposited material was on average 85 HV, increasing to around 150 HV in the HAZ and 160 HV in the unaffected base material. The loss in hardness and the extent of the HAZ is influenced by the laser power and heat input (Çam and İpekoğlu, 2016).The thickness of the HAZ appears to be around 1000 μm and closer to 1500 μm for a laser power of 2700 W and 2800 W, respectively in light of Fig. 9(c). The AA7475 base material has a high heat conductivity coefficient and thus, a softening and the formation of a HAZ is expected. This corresponds to the observation made by Li et al. (Li et al., 2018) for the closely related AA7075 alloy. It should be ephasised that the extent of the HAZ is influenced by the thickness of the base material, which was 30 mm in the current study, ensuring efficient cooling of the deposited material, limiting the extent of the zone.

In general, the hardness in the deposited material is low. As both AA2065 and AA7475 are heat-treatable alloys, attempts should be made to increase the hardness and thus, the corresponding mechanical properties by conducting a post-deposition heat treatment comprised of solution heat treatment and aging. The positive effect of such heat treatment was demonstrated by for instance Malikov et al. (Malikov et al., 2019), for laser welded Al-2.8Cu-1.8Li joints, laying the

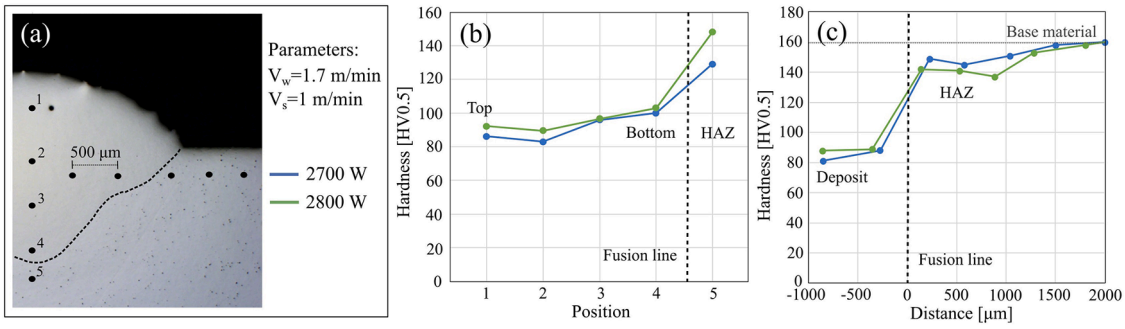

Fig. 9. (a) Illustration of the position of the hardness indents. Hardness measurements one week after deposition; (b) inside the deposited material and (c) across the deposited material and into the base material.

foundation for future work.

Conclusions

In this paper, the weldability of aerospace-grade AA2065, Al-Cu-Li alloy was evaluated through the production of single tracks by wire-feed LMD. The influence of process parameters in deposition geometry, microstructure, porosity and hardness was evaluated.

- The laser power significantly influences the geometry and surface morphology of the deposited track. The laser power determines the heat available for melting of both the wire and the base material. A too high laser power (2800 W, equal to an energy density of 5.6 J/mm^2) resulted in an unstable process causing ripples on the surface.
- Porosity is observed in the deposited tracks, however to a low extent and was for the most part related to process instabilities or excessive shield gas rate.
- Solidification cracking was not observed to be a challenge during laser metal deposition of the AA2065 wire when controlling the relationship between scanning speed and wire-feed rate.
- The microstructure consisted of columnar grains growing from the fusion zone and globular grains in the center of the deposited track. A network of a Cu-rich second phase was observed throughout the deposited material. The phase was enriched with Zn and Mg, from AA7475 close to the fusion boundary.
- Defect-free tracks with a high height/depth ratio and minimal surface rippling could be produced with a laser power of 2700 W and scanning speed of 1 m/min, giving an energy density of 5.4 J/mm^2 for wire-feed rates between 1 and 1.9 m/min.

In sum, the presented results show that it is possible to use AA2065 wires for welding purposes without the excessive formation of pores or cracks when the optimal process parameters are chosen. The presented results can contribute to finding new areas of application and production processes for utilizing Al-Cu-Li alloys. Further work should focus on the effect of heat treatment on the hardness, microstructure and corresponding mechanical properties.

Funding

This study was funded by SINTEF AS.

Availability of data and materials

The author declares that all data supporting the findings in the study are available within the article.

Code availability

Not applicable.

Ethics approval

Not applicable.

Consent to participate

Not applicable.

Consent for publication

The authors consent to publish this article.

CRediT authorship contribution statement

Siri Marthe Arbo: Conceptualization, Methodology, Investigation, Formal analysis, Writing – original draft, Project administration. **Stanka Tomovic-Petrovic:** Conceptualization, Investigation, Writing – review & editing. **Jo Aunemo:** Methodology, Investigation, Writing – review & editing. **Nora Dahle:** Methodology, Investigation, Formal analysis, Writing – review & editing. **Ola Jensrud:** Supervision, Conceptualization, Writing – review & editing.

Declaration of Competing Interest

The authors declare that they have no known competing financial interests or personal relationships that could have appeared to influence the work reported in this paper.

Acknowledgements

The authors are grateful for the help with the wire production by KA Rasmussen. The authors acknowledge the permission to publish the present work, financed by SINTEF AS.

References

Abd El-Aty, A., Xu, Y., Guo, X., Zhang, S.H., Yan, M., Chen, D., 2018. Strengthening mechanisms, deformation behavior, and anisotropic mechanical properties of Al-Li alloys: a review. J. Adv. Res. 10, 49–67. https://doi.org/10.1016/j.jare.2017.12.004.

Ahmed, B., Wu, S.J., 2014. Aluminum lithium alloys (Al-Li-Cu-X)-new generation material for aerospace applications. Appl. Mech. Mater. 440, 104–111. https://doi.org/10.4028/www.scientific.net/AMM.440.104.

Caiazzo, F., Alfieri, P.A., Sergi, V., 2017. Additive manufacturing by means of laser-aided directed metal deposition of 2024 aluminium powder: investigation and optimization. Adv. Mech. Eng. 9 (8) https://doi.org/10.1177/1687814017714982.

Çam, G., İpekoğlu, G., 2016. Recent developments in joining of aluminum alloys. Int. J. Adv. Manuf. Technol. 91 (5–8), 1851–1866. https://doi.org/10.1007/s00170-016-9861-0.

Campbell Jr, F.C., 2011. Chapter 2 – aluminum. In: Campbell Jr, FC (Ed.), Manufacturing Technology for Aerospace Structural Materials. Elsevier Science, pp. 15–92.

Dursun, T., Soutis, C., 2014. Recent developments in advanced aircraft aluminium alloys. Mater. Design (1980-2015) 56, 862–871. https://doi.org/10.1016/j.matdes.2013.12.002.

Froend, M., Riekehr, S., Kashaev, N., Klusemann, B., Enz, J., 2018. Process development for wire-based laser metal deposition of 5087 aluminium alloy by using fibre laser. J. Mater. Process Technol. 34, 721–732. https://doi.org/10.1016/j.jmapro.2018.06.033.

Gu, C., Wei, Y., Zhan, X., Zhang, D., Ren, S., Liu, H., Li, H., 2016. Investigation of welding parameters on microstructure and mechanical properties of laser beam-welded joint of 2060 Al–Cu–Li alloy. Int. J. Adv. Manuf. Technol. 91 (1–4), 771–780. https://doi.org/10.1007/s00170-016-9806-7.

Gumbmann, E., De Geuser, F., Sigli, C., Deschamps, A., 2017. Influence of Mg, Ag and Zn minor solute additions on the precipitation kinetics and strengthening of an Al-Cu-Li alloy. Acta Mater. 133, 172–185. https://doi.org/10.1016/j.actamat.2017.05.029.

Huang, W., Chen, S., Xiao, J., Jiang, X., Jia, Y., 2021. Laser wire-feed metal additive manufacturing of the Al alloy. Opt. Laser Technol. 134 https://doi.org/10.1016/j.optlastec.2020.106627.

Jiao, S., Chen, X., Shen, S., Wang, X., He, B., Liu, D., Wang, H., 2020. Microstructure evolution and mechanical behavior of Al–Li alloy fabricated by laser melting deposition technique. J. Alloys Compd. 821 https://doi.org/10.1016/j.jallcom.2019.153125.

Kim, H.T., Nam, S.W., Hwang, S.H., 1996. Study on the solidification cracking behaviour of high strength aluminum alloy welds: effect of alloying elements and solidification behaviours. J. Mater. Sci. 31 https://doi.org/10.1007/BF00355993.

Li, S., Xu, W., Xiao, G., Chen, B., 2018. Weld formation in laser hot-wire welding of 7075 aluminum alloy. Metals (Basel) 8 (11). https://doi.org/10.3390/met8110909.

Liu, F., Zhou, B., Mao, Y., Huang, C., Chen, Y., Wang, Z., 2017. Microstructure and mechanical properties of laser welded joints between 2198/2060 Al–Li alloys. Mater. Sci. Technol. 34 (1), 111–122. https://doi.org/10.1080/02670836.2017.1365221.

Madhusudhan Reddy, G., Gokhale, A.A., 2014. Chapter 9 - welding aspects of aluminum–lithium alloys. In: Prasad, NE, Gokhale, AA, Wanhill, RJH (Eds.), Aluminum-lithium Alloys: Processing, Properties, and Applications. Butterworth-Heinemann Elsevier, Boston, pp. 259–302.

Malikov, A., Orishich, A., Golyshev, A., Karpov, E., 2019. Manufacturing of high-strength laser welded joints of an industrial aluminum alloy of system Al-Cu-Li by means of post heat treatment. J. Manuf. Process 41, 101–110. https://doi.org/10.1016/j.jmapro.2019.03.037.

Molian, P.A., Srivatsan, T.S., 1990. Weldability of aluminium-lithium alloy 2090 using laser welding. J. Mater. Sci. 25.

National Aeronautics and Space Administration (2005) NASA facts, super lightweight external tank. FS-2005-04-025-MSFC. PUB 8-40341. https://www.nasa.gov/sites/default/files/113020main_shuttle_lightweight.pdf.

Rioja, R.J., Liu, J., 2012. The evolution of Al-Li base products for aerospace and space applications. Metall. Mater. Trans. A 43 (9), 3325–3337. https://doi.org/10.1007/s11661-012-1155-z.

Ryan, E.M., Sabin, T.J., Watts, J.F., Whiting, M.J., 2018. The influence of build parameters and wire batch on porosity of wire and arc additive manufactured aluminium alloy 2319. J. Mater. Process Technol. 262, 577–584. https://doi.org/10.1016/j.jmatprotec.2018.07.030.

Xiao, R., Zhang, X., 2014. Problems and issues in laser beam welding of aluminum–lithium alloys. J. Manuf. Process 16 (2), 166–175. https://doi.org/10.1016/j.jmapro.2013.10.005.

Xu, X., Mi, G., Luo, Y., Jiang, P., Shao, X., Wang, C., 2017. Morphologies, microstructures, and mechanical properties of samples produced using laser metal deposition with 316 L stainless steel wire. Opt. Laser Eng. 94, 1–11. https://doi.org/10.1016/j.optlaseng.2017.02.008.

Zhang, X., Huang, T., Yang, W., Xiao, R., Liu, Z., Li, L., 2016. Microstructure and mechanical properties of laser beam-welded AA2060 Al-Li alloy. J. Mater. Process Technol. 237, 301–308. https://doi.org/10.1016/j.jmatprotec.2016.06.021.

Zhang, Y., Tao, W., Chen, Y., Nan, T., 2020. Effects of heat treatment on microstructure and mechanical properties of double-sided laser-welded AA2060/AA2099 T-joint. J. Mater. Process Technol. 285 https://doi.org/10.1016/j.jmatprotec.2020.116777.

Zhong, H., Qi, B., Cong, B., Qi, Z., Sun, H., 2019. Microstructure and mechanical properties of wire + arc additively manufactured 2050 Al–Li alloy wall deposits. Chin. J. Mech. Eng. 32 (1) https://doi.org/10.1186/s10033-019-0405-z.